# Multispectral elastic scanning lidar for industrial flare research: characterizing the electronic subsystem and application

**Juan Luis Guerrero-Rascado,[1,2,3,*] Renata Facundes da Costa,[3] Andrés Esteban Bedoya,[4] Roberto Guardani,[5] Lucas Alados-Arboledas,[1,2] Álvaro Efrain Bastidas,[4] and Eduardo Landulfo[3]**

[1]*Instituto Interuniversitario de Investigación del Sistema Tierra en Andalucía (IISTA-CEAMA), Av. del Mediterráneo, 18006, Granada, Spain*
[2]*Dpto. Física Aplicada, Universidad de Granada, Fuentenueva s/n, 18071, Granada, Spain*
[3]*Centro de Lasers e Aplicações, Instituto de Pesquisas Energéticas e Nucleares (IPEN), Avd. Prof. Lineu Prestes 2242, 05508-000, São Paulo, Brazil*
[4]*Escuela de Física, Universidad Nacional de Colombia, Calle 59ª Nº 63-20, Medellín, Colombia*
[5]*Dpto. Engenheria Química, Universidade de São Paulo, Av. Luciano Gualberto, 380 Trav. 3, 05508-900, São Paulo, Brazil*
[*]*rascado@ugr.es*

**Abstract:** This work deals with the analysis of the electronic subsystem of a multiwavelength elastic scanning lidar. Several calibration tests are applied to the Cubatão scanning lidar placed at the industrial area of Cubatão in the State of São Paulo (Brazil), in order to improve the knowledge of its performing itself and to design protocols for correcting lidar signal for undesirable instrumental effects. In particular, the trigger delay is assessed by means of zero-bin and bin-shift tests for analog (AN) and photo-counting (PC) signals, respectively. Dark current test is also performed to detect potential range-dependency that could affect lidar products. All tests were performed at different spatial resolutions. These instrumental corrections were applied to a case study of data acquired for characterizing the optical and microphysical properties of particles in an industrial flare. To that aim, a graphical method based on the space defined by the extinction-related Angström exponent versus its spectral curvature is used to derive the contribution of fine aerosol to extinction and the size of the fine aerosols in the industrial flare, therefore revealing features of the processes occurring inside the flame. Our study demonstrates the potential of this new technique for the study and measurement of industrial emissions.



**OCIS codes:** (010.0280) Remote sensing and sensors; (010.1100) Aerosol detection; (010.1120) Air pollution monitoring; (010.3640) Lidar.

## References and links

1. P. Weibring, M. Andersson, H. Edner, and S. Svanberg, "Remote monitoring of industrial emissions by combination of lidar and plume velocity measurements," Appl. Phys. B **66**(3), 383–388 (1998).
2. U.S. Environmental Protection Agency, EPA Proposes Clean Air Standards for Harmful Soot Pollution/99 percent of U.S. counties projected to meet proposed standards without any additional actions, http://yosemite.epa.gov/opa/admpress.nsf/0/F51C2FDEDA736EA285257A1E0050C45F (2012).
3. M. J. Molina and L. T. Molina, "Megacities and atmospheric pollution," J. Air Waste Manag. Assoc. **54**(6), 644–680 (2004).
4. M. C. de Mello Lemos, "The politics of pollution control in Brazil: State actors and social movements cleaning up Cubatão," World Dev. **26**(1), 75–87 (1998).
5. CETESB, "Environmental pollution control in Cubatão: results report July 1983 to July 1986" (CETESB, 1986).
6. CETESB, "Relatório de qualidade do ar no estado de São Paulo" (CETESB, 2013).
7. J. Steffens, R. Guardani, E. Landulfo, P. F. Moreira, Jr., and R. F. da Costa, "Study on correlations between lidar scattered light signal and air quality data in an industrial area," Procedia Environ. Sci. **4**, 95–102 (2011).

#221198 - $15.00 USD Received 18 Aug 2014; revised 25 Sep 2014; accepted 25 Sep 2014; published 8 Dec 2014

8. R. F. da Costa, J. Steffens, E. Landulfo, R. Guardani, W. M. Nakaema, P. F. Moreira, Jr., F. J. S. Lopes, and P. Ferrini, "Real-time mapping of an industrial flare using LIDAR," Proc. SPIE **8182**, 81820Y (2011).
9. R. F. da Costa, R. Bourayou, E. Landulfo, R. Guardani, I. Veselovskii, and J. Steffens, "Stand-off mapping of the soot extinction coefficient in a refinery flare using a 3-wavelength elastic backscatter LIDAR," Proc. SPIE **8894**, 88940P (2013).
10. G. Pappalardo, A. Amodeo, A. Apituley, A. Comerón, V. Freudenthaler, H. Linné, A. Ansmann, J. Bösenberg, G. D'Amico, I. Mattis, L. Mona, U. Wandinger, V. Amiridis, L. Alados-Arboledas, D. Nicolae, and M. Wiegner, "EARLINET: towards an advanced sustainable European aerosol lidar network," Atmos. Meas. Tech. **7**(8), 2389–2409 (2014).
11. J. L. Guerrero-Rascado, "Técnica Lidar para la caracterización atmosférica mediante dispersión elástica y Raman," PhD. Dissertation, D.L.: GR. 187–2009 (University of Granada, 2009).
12. F. Navas-Guzmán, "Atmospheric vertical profiling by Raman lidar," PhD. Dissertation, D.L.: GR 3118–2012 (University of Granada, 2012).
13. J. A. Bravo-Aranda, "Lidar depolarization technique: assessment of the hardware polarizing sensitivity and applications," PhD. Dissertation (University of Granada, 2014).
14. V. A. Kovalev and W. E. Eichinger, *Elastic Lidar: Theory, Practice and Analysis Methods* (Wiley-Interscience, 2004).
15. F. G. Fernald, B. M. Herman, and J. A. Reagan, "Determination of aerosol height distribution by lidar," J. Appl. Meteorol. **11**(3), 482–489 (1972).
16. F. G. Fernald, "Analysis of atmospheric lidar observations: some comments," Appl. Opt. **23**(5), 652–653 (1984).
17. J. D. Klett, "Stable analytical inversion solution for processing lidar returns," Appl. Opt. **20**(2), 211–220 (1981).
18. J. D. Klett, "Lidar inversion with variable backscatter/extinction ratios," Appl. Opt. **24**(11), 1638–1643 (1985).
19. A. Ansmann, U. Wandinger, M. Riebesell, C. Weitkamp, and W. Michaelis, "Independent measurement of extinction and backscatter profiles in cirrus clouds by using a combined Raman elastic-backscatter lidar," Appl. Opt. **31**(33), 7113–7131 (1992).
20. R. J. Hall and P. A. Bonczyk, "Sooting flame thermometry using emission/absorption tomography," Appl. Opt. **29**(31), 4590–4598 (1990).
21. O. I. Smith, "Fundamentals of soot formation in flames with application to diesel engine particulate emissions," Pror. Energy Combust. Sci. **7**(4), 275–291 (1981).
22. C. H. Jung and Y. P. Kim, "Analytic solution on the estimation of the Ångstrom exponent in log-normal aerosol size distribution," Particul. Sci. Technol. **31**(1), 92–99 (2013).
23. Z. G. Habib and P. Vervisch, "On the refractive index of soot at flame temperature," Combust. Sci. Technol. **59**(4–6), 261–274 (1988).
24. M. R. Davis, "Turbulent refractive index fluctuations in a hydrogen diffusion flame," Combust. Sci. Technol. **64**(1–3), 51–65 (1989).
25. Y. J. Kaufman, "Aerosol optical thickness and atmospheric path radiance," J. Geophys. Res. **98**(D2), 2677–2692 (1993).
26. G. L. Schuster, O. Dubovik, and B. N. Holben, "Angström exponent and bimodal aerosol size distributions," J. Geophys. Res. **111**(D7), D07207 (2006).
27. G. P. Gobbi, Y. J. Kaufman, I. Koren, and T. F. Eck, "Classification of aerosol properties derived from AERONET direct sun data," Atmos. Chem. Phys. **7**(2), 453–458 (2007).
28. M. R. Perrone, F. de Tomasi, and G. P. Gobbi, "Vertically resolved aerosol properties by multi-wavelength lidar measurements," Atmos. Chem. Phys. **14**(3), 1185–1204 (2014).

## 1. Introduction

The emission of pollutants in megacities and industrial areas can have strong impact, not only from an environmental point of view, but also for human health. Microscopic particles can penetrate deep into the lungs and have been linked to a wide range of serious health effects, including premature death, heart attacks, and strokes, as well as acute bronchitis and aggravated asthma among children [1, 2]. Many studies have been carried out to evaluate whether long-term exposure to air pollutants is related to mortality, leading to the conclusion that premature mortality can be associated predominantly to the presence of particulate matter [3].

Cubatão is an industrialized city located at São Paulo state coast in Brazil. During the 1980s, it was considered to be the most polluted city in the world by the United Nations, and commenced a large pollutant monitoring program until receiving the "symbol of environmental recovery" by the same international organization in the 90's. But a lot of health problems still remain.

The sluggish dispersion of air pollutants in Cubatão caused both extreme discomfort and long term health problems for the population of the region. Poor people in Cubatão lived in extremely degraded and risk-prone areas, such as polluted marshes exposed to flooding, mountain slopes subject to mudslides, and hazardous terrains in the middle of the

#221198 - $15.00 USD Received 18 Aug 2014; revised 25 Sep 2014; accepted 25 Sep 2014; published 8 Dec 2014

petrochemical complex and on top of pipelines and toxic dumps [4]. Moreover, pollution related health problems were highly common among Cubatão residents, particularly blood-related and respiratory diseases, and birth defects [4]. Although environmental degradation in Cubatão had been a serious problem since the late 50's, as pollution control was absent from the governmental agenda for more than 20 years. In 1983, however, CETESB (Companhia Estadual de TEcnologia de Saneamento Básico, the state environmental protection agency) carried out a pollution control program that significantly reduced air, water, and soil pollution in Cubatão [5, 6]. One of the sources of pollutants in the city comes from biomass burning and oil refineries. Thus, continuous and unattended air quality monitoring techniques to evaluate the quality of the combustion in industrial flares are very useful under this scenario [7].

Industrial flaring is a high-temperature oxidation process used to controllably burn combustible components, mostly hydrocarbons, of waste gases from industrial operations. Characterization of atmospheric emissions from industrial flare still represents a challenge in measurement techniques because it is extremely difficult to determine the real-time concentration of combustion products using conventional in situ sampling (due to instrumental difficulties and the dynamics of oscillations in the emission patterns) [8, 9]. Lidar is a very useful tool in atmospheric research since it provides information on several atmospheric properties with very high spatial (order of meters) and temporal resolution (order of seconds). To properly apply the lidar technique, a thorough hardware characterization must be done. In particular, its performance in the near range must be tested to get trustable information from flames.

This article is organized as follows. Section 2 presents the features of the experimental site and the lidar technical specifications. Section 3 describes the different tools used to characterize the electronic system of the Cubatão lidar. Section 4 is devoted to results and to assessing the performing of the lidar. A case study of characterization of optical and microphysical properties in a flame is shown. Finally, Section 5 summarizes the conclusions of this study.

## 2. Experimental site and instrumentation

Experimental data were acquired at CEPEMA (Centre for Training and Research in Environment), located at the industrial area of Cubatão (23° 53′ S, 46° 26′ W, 10 m asl). Cubatão is located in a narrow coastal plain surrounded by a steep mountain range to the north, west, and east, and by the sea to the south. At about 1 km west and northwest a 600-1000 m high mountain shell restrains air circulation. It is one of the largest industrial sites in the country. In a region of about 40 $km^2$ there are twenty-three large industry complexes, including a steel plant, oil refinery, seven fertilizer plants, a cement plant, and eleven chemical/petrochemical plants, adding up to two hundred and sixty pollutant emission sources. Furthermore, the urban area includes around one hundred and thirty thousand inhabitants [7].

The scanning lidar system acquiring the data set is located at CEPEMA in Cubatão, installed approximately 400 m from a Petrobras oil refinery flare stack. This flare stack has a total height of approximately 40 m relative to the ground level. Localization of the lidar system at CEPEMA and flare stack sites is shown in Fig. 1. This lidar is a multiwavelength elastic system with scanning capability and biaxial configuration (Fig. 2). The laser source is a commercial Nd:YAG laser (CFR 450, Quantel SA) operating at 355, 532 and 1064 nm, with a fixed repetition rate of 20 Hz and energies per pulse between 100 and 400 mJ. The receiving module is a 150 mm diameter Dall-Kirkham telescope and focal length of 1000 mm which collects the backscattered laser light. It is currently used with a fixed field-of-view (FOV) of 1 mrad, which permits a full overlap between the telescope FOV and the laser beam at range around 120 m. This FOV value, together with the detection electronics, enables sampling at distances up to 7 km, both day and night time.

#221198 - $15.00 USD Received 18 Aug 2014; revised 25 Sep 2014; accepted 25 Sep 2014; published 8 Dec 2014


Fig. 1. Location of the industrial and residential areas at Cubatão, and the scanning lidar system installed at CEPEMA.

Fig. 2. Cubatão scanning lidar in operation during the sampling sequence of the flare.

The backscattered laser radiation is detected by two photomultiplier tubes (Hamamatsu) for 355 and 532 nm, and one Si-avalanche photodiode (EG&G) for 1064 nm, coupled to narrowband interference filters to assure the reduction of the solar background during daytime operation and improve the signal-to-noise ratio. The detected signals are recorded by a transient recorder in both analog (AN) and photocounting (PC) mode with selectable spatial resolutions of 3.75, 7.5, 15 and 30 m. The laser and telescope devices are attached to a scanning base adapted from a 2AP (2-axis positioner) sun tracker (Kipp & Zonnen) that performs changes in both azimuthal and polar angles, with an accuracy of less than 0.02°.This system has two stepper motors controlled by an on-board micro-computer to program a full scanning over a desired angle range.

## 3. Methodology

Different tests, routinely applied in EARLINET (European Aerosol Research Lidar Network, www.earlinet.org) [10] have been conducted for detecting potential anomalies in the performing of the electronic subsystem of the Cubatão scanning lidar. A detailed description of these tests can be found in the literature (e.g. see [11–13]). However, a summary is given in the following subsections:

#221198 - $15.00 USD Received 18 Aug 2014; revised 25 Sep 2014; accepted 25 Sep 2014; published 8 Dec 2014

### *3.1 Zero-bin calibration*

Lidar instruments use a trigger device for a dual purpose, which is to simultaneously activate the pulse-firing mechanism and data acquisition by a transient recorder. Nevertheless, lidar system can exhibit a certain temporal delay between both activations and, in turn, a certain spatial displacement respect to the real position of the target. Consequently, this distorts the lidar signal detected by the instrument and it will impact on any lidar-derived product.

To assess the existence of this spatial displacement, the backscattered signal by a target located in the near range at a known distance from the lidar is used. In this study, a black cardboard placed at approximately 40 cm from the instrument was used. Measurements of 1 min were performed for zero-bin calibration at all channels. Because it was placed at distance less than the nominal spatial resolution, such strong backscattered signal should be detected at bin #0 (initial bin). Otherwise, its detection at a different bin will indicate the presence of a certain trigger delay. Figure 3 illustrates the zero-bin calibration for channel 532 nm in AN mode. A strong peak is observed at bin #10, revealing the existence of a non-negligible trigger delay for this channel.

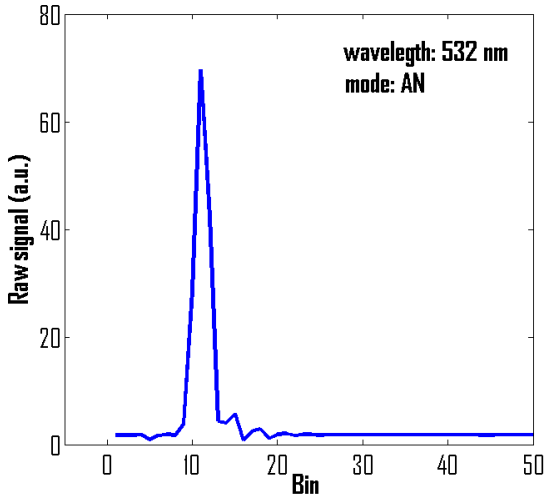


Fig. 3. Zero-bin calibration at 532 nm in AN mode indicating a delay between the laser pulses firing and the start of data acquisition.

### *3.2 Bin-shift calibration*

Due to PC signals typically saturating in the near-range, the calibration described in Section 3.1 does not allow for unambiguously determining the zero-bin position for these channels. An indirect procedure, the so-called bin-shift calibration, is employed to determine the zero-bin for PC signals. This procedure is based on the comparison of the shape of AN and PC signals, so that both signals should simultaneously detect atmospheric targets at the same distance for an ideal system. This calibration procedure determines the bin-shift by the best linear fit in a certain distance range between AN and PC signals (using AN signal as a reference), sliding the PC signal around it (Fig. 4). The bin-shift value is found as the sliding with the best correlation coefficient. In this study a 10-min measurement and a sliding window between –20 and + 20 bins were used.

Finally, the zero-bin for PC signals can be derived from Eq. (1):

$$bin_0^{PC} = bin_0^{AN} + \Delta bin_{AN-PC}. \quad (1)$$

#221198 - $15.00 USD Received 18 Aug 2014; revised 25 Sep 2014; accepted 25 Sep 2014; published 8 Dec 2014

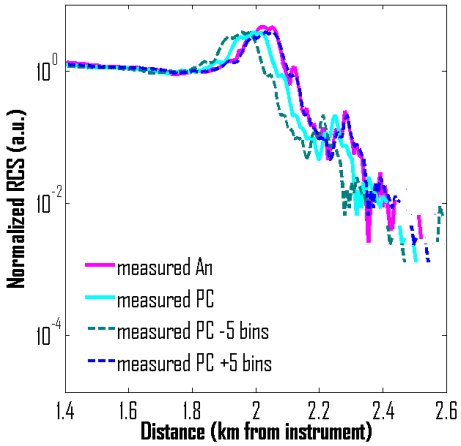


Fig. 4. Bin-shift calibration at 355 nm by comparison of AN (pink) and PC (cyan) signals. AN signal is fixed and PC signals is slided between −5 (dashed dark cyan) and + 5 bins (dashed blue). Both signals matches when PC signal is displaced 5 bins to the right.

### *3.3 Dark current measurement*

Dark current is the response exhibited by a receptor of radiation during periods when it is not actively illuminated. This current flows because the material used as the photocathode has low work functions, therefore being able to emit thermal electrons even at room temperature. The magnitude of the dark current depends on the photocathode material, the temperature of the tube and the applied voltage [14].

The dark current measurement consist of a measurement taken by covering totally the telescope or detectors (to avoid that any radiation achieves the optical subsystem) performed with enough averaging time. To perform the dark current test, it is necessary that all parameters of measurements, as voltage applied to detectors and frequency of repetition of pulses among others, are configured as a usual measurement. In addition, it must pay special attention to any portion of laser radiation reaches the detectors. In that way, any signal distortion and stray-light peaks observed will not come from the interaction between radiation and atmosphere but they will come from the instrument itself. Dark current measurement was performed over 10 min.

### *3.4 Retrieval of flame optical properties*

To characterize the emissions from an industrial flare stack, a 12x12 virtual matrix is used to discretize the flare region with respect to the lidar. The measurement sequence was designed forming a zig-zag to minimize the total acquisition time (starting from the lower left cell) with variations of the zenithal and azimuthal angles in steps of 0.02° and 0.03°, respectively, and performing 10-s measurements at each matrix cell. The variations of the zenithal and azimuthal angles were made in steps of 0.02° and 0.03°, respectively. Lidar signal at a given distance from the system is expressed as:

$$R.C.S.(\lambda) = KO(r)\beta(\lambda)e^{-2\int_{r_0}^{r}\alpha(\zeta,\lambda)d\zeta}. \qquad (2)$$

where R.C.S.(λ) is the range corrected lidar signal (i.e., signal corrected for dark-current, zero-bin, background and range-squared distance at the wavelength λ), K is an instrumental constant accounting for the effective telescope area, pulse length and optical efficiency, O(r) is the overlap function, which reports on the geometrical overlap between the laser beam and the telescope field of view depending on the distance r from the lidar system, and β(λ) is the atmospheric backscatter coefficient for both molecules and particle flame contributions. Note thus β(λ) in Eq. (2) is only wavelength-dependent due to being evaluated at a given distance r

#221198 - $15.00 USD Received 18 Aug 2014; revised 25 Sep 2014; accepted 25 Sep 2014; published 8 Dec 2014

from the lidar. $r_1$ and $r_2$ are the leading edge and trailing edge of the flame, respectively. $\alpha(\zeta,\lambda)$ is the atmospheric extinction coefficient (molecules plus particle flame contribution), which depends on the wavelength and the traveling distance $\zeta$.

Forming a ratio at the leading and trailing edge of the flame, Eq. (2) can be written as

$$\frac{R.\mathrm{C.S.}(r_1,\lambda)}{R.\mathrm{C.S.}(r_2,\lambda)} = e^{-2\int_{r_2}^{r_1}\alpha(\zeta,\lambda)d\zeta} = e^{-2\tau_{flame}(\lambda)}. \quad (3)$$

Here, the overlap function at $r_1$ and $r_2$ are unity due to the industrial flare stack is placed at a distance (400 m from the instrument) where full overlap is achieved. The atmospheric backscatter coefficient is assumed to be equal at $r_1$ and $r_2$ (i.e., a horizontally homogeneous atmosphere is assumed around the flame). Thus, the flame optical depth, $\tau_{flame}(\lambda)$, can be determined as

$$\tau_{flame}(\lambda) = -\frac{\ln\left[\frac{R.\mathrm{C.S.}(r_1,\lambda)}{R.\mathrm{C.S.}(r_2,\lambda)}\right]}{2}. \quad (4)$$

From Eq. (4), the particle extinction coefficient, assuming homogeneity between $r_1$ and $r_2$, is:

$$\alpha_{part}(\lambda) = \frac{\tau_{flame}(\lambda)}{r_2 - r_1} - \alpha_{mol}(\lambda). \quad (5)$$

where $\alpha_{mol}(\lambda)$ is the molecular extinction coefficient, calculated from Rayleigh theory where temperature and pressure are known. Finally, the extinction-related Angström exponent, which provides information about the predominance of fine/coarse particles, is computed as

$$AE_{\lambda_1,\lambda_2} = -\frac{\ln\left[\frac{\alpha_{part}(\lambda_1)}{\alpha_{part}(\lambda_2)}\right]}{\ln\left[\frac{\lambda_1}{\lambda_2}\right]}. \quad (6)$$

## 4. Results and discussion

### *4.1. Instrumental tests*

Data reported in this work were acquired under four different spatial resolutions (i.e., at 3.75, 7.5, 15 and 30 m) in order to check the instrumental characterization at each setting. The zero-bin test was performed several times to verify the reproducibility of this calibration. As can be seen in Table 1, a displacement of the zero-bin position is observed for all AN channels and spatial resolutions selected. Because lidar fundamentals are based on a timing technique (which in turn is converted into a ranging technique through the light velocity), the temporal delay between the laser beam emission and start of data acquisition is converted to a different number of bins when different spatial resolutions are used. For the Cubatão scanning lidar the zero-bin position is located at bins #10 and #11 (depending on wavelength) when the maximum spatial resolution is used, decreasing up to bin #1 at 30-m spatial resolution.

**Table 1.** Zero-bin position for AN channels determined experimentally using different spatial resolutions[a]

| Spatial resolution (m) | Zero-Bin Position (AN channels) | | |
|---|---|---|---|
| | 355 nm | 532 nm | 1064 nm |
| 3.75 | 11 (-) | 10 (-) | 10 (-) |
| 7.5 | 5 (5) | 5 (5) | 5 (5) |
| 15 | 2 (2) | 2 (2) | 2 (2) |
| 30 | 1 (1) | 1 (1) | 1 (1) |

[a]Theoretical values (obtained from the application of Eq. (7) using the seed value given by the maximum spatial resolution) are included in brackets.

#221198 - $15.00 USD Received 18 Aug 2014; revised 25 Sep 2014; accepted 25 Sep 2014; published 8 Dec 2014

The displacement of the zero-bin position as spatial resolution changes can be easily understood taking into account the size of each bin under different spatial resolution (Fig. 5). For example, if a target is placed in the distance-range 52.50-56.25 m from the lidar, it will be detected at bin #13 if spatial resolution of 3.75 m is used. Simultaneously, this target located at the same position is detected at bin #6, #3 and #1 when spatial resolutions of 7.5, 15 and 30 m are selected, respectively. From the inspection of Fig. 5, an equation relating the zero-bin position at different spatial resolutions can be inferred as

$$bin_0(\mathrm{n}) = \mathrm{integer}\left[\frac{bin_0(\mathrm{n}=0)}{2^n}\right]. \quad (7)$$

where the values of n = 0,1,2,3 determine the different spatial resolutions (resolution(n) = $3.75 \cdot 2^n$). For comparison, Table 1 also contains, in brackets, the theoretical values obtained from the application of Eq. (7) using the seed value given by the maximum spatial resolution (i.e. spatial resolution of 3.75 m). As it can be seen, Eq. (6) is exactly fulfilled by the experimental results. Therefore, the theoretical determination of the zero-bin position at different spatial resolutions is feasible from the experimental knowledge of the zero-bin position at the maximum spatial resolution.

As result of the application of the zero-bin calibration for several days and several spatial resolutions, it can be concluded that to properly use the lidar signals in any lidar procedure (i.e. derivation of range corrected signals plots, Klett-Fernald method [15–18] and Raman algorithm [19], among others) some bins of the AN signals (depending on wavelength and the selected spatial resolution) must be removed following Table 1. The zero-bin calibration was attempted for the PC channels using the procedure described in Section 3.1. However, the saturation observed in the PC signals did not allow us to unambiguously determine the zero-bin position for these channels and it was necessary to perform the bin-shift calibration described in Section 3.2.

Orographic conditions surrounding the area of study with mountains of relatively low altitude (600-1000 m asl) led to low clouds formation, typically below 1000 m asl. Because the bin-shift calibration requires a distance-range where both AN and PC properly detect atmospheric structures (such as aerosol layers or clouds) simultaneously, the Cubatão scanning lidar was operated at a zenith angle of 25° to guarantee profiling a target at 1.5-2.5 km from the system. This calibration takes around 10 min at each spatial resolution and, due to the high variability of the cloud field, different clouds were used as targets.

Figure 6 illustrates the bin-shift calibration at 355 nm performed on 20/05/2014 from 16:07 to 16:17 (local time) with a spatial resolution of 7.5 m. As can be seen on the upper plot, there is a certain displacement between the range corrected signal in AN mode (without correction for zero-bin calibration) and the corresponding range corrected signal in PC mode. This displacement is clearly visible in the distance-range where a cloud was detected (between 2.4 and 2.8 km above the instrument). The lower plot contains the correlation coefficients of range corrected signal in AN mode versus range corrected signal in PC mode, computed on a certain range of interest (where the cloud was detected) and displacing the PC signal between −20 and + 20 bins with respect to the AN signal. In the case shown in Fig. 6, the highest correlation coefficient was found when the PC signal was placed 5 bins below the corresponding AN signals or, alternatively, when the bin-shift is −5 bins. Combining the zero-bin calibration reported in Table 1 and this bin-shift calibration, Eq. (1) determines a zero-bin position for PC signal of 0 bins.

#221198 - $15.00 USD Received 18 Aug 2014; revised 25 Sep 2014; accepted 25 Sep 2014; published 8 Dec 2014

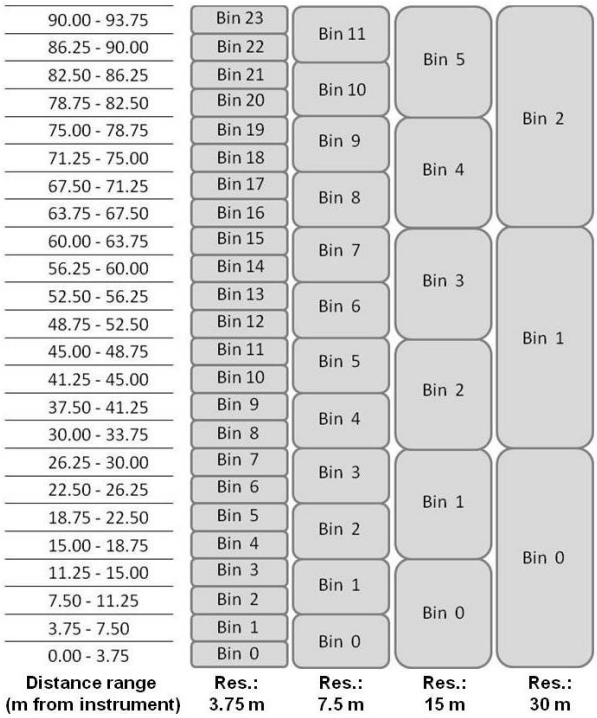


Fig. 5. Relationship between distance-ranges from lidar and the corresponding bins using different spatial resolutions.

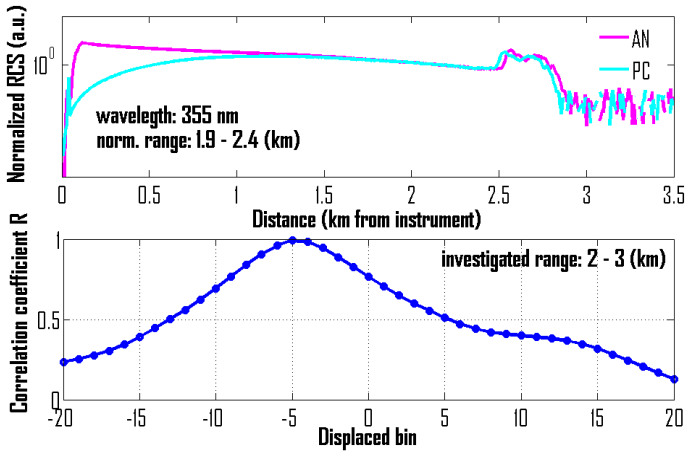


Fig. 6. Bin-shift calibration at 355 nm performed on 20/05/2014 between 16:07 and 16:17 (local time) at spatial resolution of 7.5 m: (upper panel) normalized range corrected signals in AN and PC modes (normalization distance range: 1.5-2.4 km above the instrument) and (bottom panel) correlation coefficient between An and PC range corrected signals (evaluated in the distance range between 2 and 3 km above the instrument) fixing the AN signal and displacing the PC signal between –20 and + 20 bins.

Bin-shift calibration was performed under three different scenarios, which allows us to verify the reproducibility of this calibration. Table 2 collects the bin-shift between AN and PC signals and the derived bin-shift for PC mode at the different wavelengths and spatial resolutions. As it can be seen, all bin-shifts were found to be negative, meaning all PC signals are displaced several bins towards the instrument (with respect to the AN signals). Similarly to the zero-bin calibration, the bin-shift values are dependent on the spatial resolution,

#221198 - $15.00 USD Received 18 Aug 2014; revised 25 Sep 2014; accepted 25 Sep 2014; published 8 Dec 2014

showing smaller values as spatial resolution decreases. Thus, bin-shift ranges between −9 bins at a spatial resolution of 3.75 m and −1 bin at a spatial resolution of 30 m (at 355 and 532 nm). The extremely poor signal-to-noise ratio for the channel 1064 nm in PC mode at any selected spatial resolution prevented the proper application of this test, and reliable conclusions could not be achieved for this channel. After knowing the bin-shift, the zero-bin position for all PC channels was determined using Eq. (6) as #0 bins for most of them, demonstrating synchronous laser beam emission and start of data acquisition (temporal delay equal to zero). Only some PC channels (i.e., 355 and 532 nm) with spatial resolutions of 3.75 m and 532 nm with spatial resolution of 15 m, exhibited values between #1 and #2 bins. Those positive values mean that some bins of these PC signals must be removed, following Table 2.

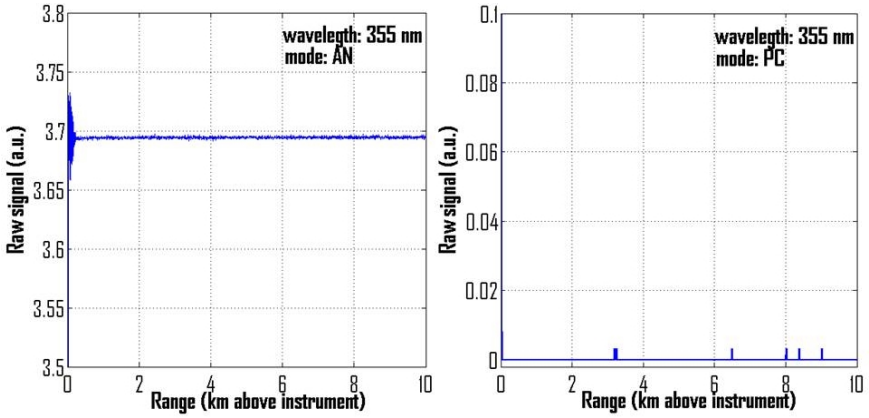


Fig. 7. Dark current measurement performed over 10 min at 355 nm with spatial resolution of 3.75 m: (left) AN mode and (right) PC mode.

Dark current measurements at different spatial resolutions were performed over 10 min, taking into account the zero-bin positions determined previously. As expected, AN and PC modes showed different behavior. Figure 7 shows the dark current measurement at 355 nm in AN and PC modes at 3.75m-resolution. AN dark current was constant with positive values for the entire distance range sounded, except very close to the instrument where stray-light peaks are detected up to 250 m from the instrument. PC dark current showed an expected value of zero in most of the distance range. Some spurious photons were counted along the profile but impact on the lidar retrievals is assumed to be negligible.

**Table 2. Zero-bin position for AN channels and bin-shift between AN and PC channels determined experimentally and zero-bin position for PC channels resulting from application of Eq. (6) for 355 and 532 nm using different spatial resolutions**

| Spatial resolution: 3.75 m | | | |
|---|---|---|---|
| Channel (nm) | Zero-bin AN (bins) | Bin-shift (bins) | Zero-bin PC (bins) |
| 355 | 11 | –9 | 2 |
| 532 | 10 | –9 | 1 |
| Spatial resolution: 7.5 m | | | |
| Channel (nm) | Zero-bin AN (bins) | Bin-shift (bins) | Zero-bin PC (bins) |
| 355 | 5 | –5 | 0 |
| 532 | 5 | –5 | 0 |
| Spatial resolution: 15 m | | | |
| Channel (nm) | Zero-bin AN (bins) | Bin-shift (bins) | Zero-bin PC (bins) |
| 355 | 2 | –2 | 0 |
| 532 | 2 | –1 | 1 |
| Spatial resolution: 30 m | | | |
| Channel (nm) | Zero-bin AN (bins) | Bin-shift (bins) | Zero-bin PC (bins) |
| 355 | 1 | –1 | 0 |
| 532 | 1 | –1 | 0 |

#221198 - $15.00 USD Received 18 Aug 2014; revised 25 Sep 2014; accepted 25 Sep 2014; published 8 Dec 2014

The near field is especially relevant for the Cubatão scanning lidar because it is used for flame application to investigate a tower placed at 400 m from the instrument. Therefore, a correct characterization of the near field is particularly important, and dark current was analyzed in two different distance ranges for all wavelengths at different spatial resolutions: 0-300 m (distance ranges containing spurious peaks) and above 300 m (distance ranges without spurious peaks and containing the target of interest) (Table 3).

For AN mode, mean dark currents are similar when comparing near and distance range (for a given wavelength and mode). However, the standard deviation substantially decreases in the range above 0.3 km (more than 50%). This is a good measurement of the range-independency of the dark current above 0.3 km, which is the range typically used for the application of this instrument. The near range shows larger variability of dark current for AN mode indicating that the lidar signal must be properly corrected for this behavior before the application of any lidar algorithm. Results at all distance ranges indicate an appropriate performing of PC mode at 355 and 532 nm, with values statistically matching zero.

**Table 3. Mean value (±standard deviation) of 10-min dark current measurements performed at 355, 532 and 1064 nm with different spatial resolutions for near and far distance ranges**

| Resolution (m) | Range (m) | Dark current at 355 nm (a.u.) | |
|---|---|---|---|
| | | AN | PC |
| 3.75 | 0.0-0.3 | 3.693 ± 0.013 | 0.0002 ± 0.0019 |
| | > 0.3 | 3.6948 ± 0.0008 | 0.00001 ± 0.00017 |
| 7.5 | 0.0-0.3 | 3.703 ± 0.010 | 0.0001 ± 0.0005 |
| | > 0.3 | 3.7043 ± 0.0006 | 0.00002 ± 0.00017 |
| 15 | 0.0-0.3 | 3.7037 ± 0.0023 | 0.0001 ± 0.0003 |
| | > 0.3 | 3.7049 ± 0.0005 | 0.00002 ± 0.00014 |
| 30 | 0.0-0.3 | 3.6984 ± 0.0015 | 0.00004 ± 0.00013 |
| | > 0.3 | 3.6997 ± 0.0004 | 0.00002 ± 0.00009 |
| Resolution (m) | Range (m) | Dark current at 532 nm (a.u.) | |
| | | AN | PC |
| 3.75 | 0.0-0.3 | 1.614 ± 0.008 | 0 ± 0 |
| | > 0.3 | 1.6134 ± 0.0020 | 0.0000 ± 0.0003 |
| 7.5 | 0.0-0.3 | 1.611 ± 0.003 | 0 ± 0 |
| | > 0.3 | 1.6105 ± 0.0006 | 0.00002 ± 0.00019 |
| 15 | 0.0-0.3 | 1.6094 ± 0.0016 | 0 ± 0 |
| | > 0.3 | 1.6086 ± 0.0005 | 0.00002 ± 0.00013 |
| 30 | 0.0-0.3 | 1.6126 ± 0.0012 | 0 ± 0 |
| | > 0.3 | 1.6120 ± 0.0004 | 0.00002 ± 0.00011 |
| Resolution (m) | Range (m) | Dark current at 1064 nm (a.u.) | |
| | | AN | PC |
| 3.75 | 0.0-0.3 | 11.3 ± 0.3 | 2.04 ± 9.61 |
| | > 0.3 | 11.281 ± 0.003 | 0.009 ± 0.005 |
| 7.5 | 0.0-0.3 | 11.29 ± 0.15 | 2.58 ± 10.14 |
| | > 0.3 | 11.282 ± 0.003 | 0.008 ± 0.004 |
| 15 | 0.0-0.3 | 11.29 ± 0.04 | 2.57 ± 9.65 |
| | > 0.3 | 11.2956 ± 0.0017 | 0.0078 ± 0.0027 |
| 30 | 0.0-0.3 | 11.306 ± 0.014 | 2.57 ± 8.06 |
| | > 0.3 | 11.3114 ± 0.0011 | 0.0074 ± 0.0017 |

To compute the mean values in the distance range 0.0-0.3 km some of the first bins were not taken into account because they were anomalously high. Concretely the first bin was neglected from dark current measurement at 355 nm in PC mode at resolutions 7.5, 15 and 30 m and also from dark current measurement at 532 in PC at resolutions 15 and 30 m. In addition, the first 4 and 3 bins were neglected from dark current at 532 nm in PC mode at resolutions of 3.75 and 7.5 m. The impact of such bins on the broader analysis is assumed to be negligible due to: (i) these bins being located very close to the instrument where the overlap function presents values equal to zero, and therefore they are not considered in most of the lidar products and (ii) typical signals in PC mode are not used in the near field due to saturation. The non-zero values of the channel 1064 nm in PC mode clearly reveals the

#221198 - $15.00 USD Received 18 Aug 2014; revised 25 Sep 2014; accepted 25 Sep 2014; published 8 Dec 2014

inappropriate performance of this channel, as was previously observed in the bin-shift calibration.

*4.2 Mapping particle optical and microphysical properties of refinery flames: a case study*

On 15 July 2014 measurements using a spatial resolution of 7.5 m were acquired to characterize the optical properties of an industrial flame at Cubatão, following the scheme described in Section 3.4. Figure 8 (upper row) shows the intensity of the lidar R.C.S. at 355, 532 and 1064 nm on the virtual-monitored matrix at the flame position (after applying all instrumental corrections). Values at each virtual pixel were computed as the mean value of 5 bins along the lidar line-of-sight. Large values of R.C.S. are observed in ~20% of the examined pixels, allowing to better identification of flame boundaries at larger wavelengths. Application of Eqs. (5) and (6) on the range 367.5-397.5 m (bins 49-53) provides the particle extinction coefficient and extinction-related Angström exponent along the virtual monitoring matrix (Fig. 8 middle and bottom rows, respectively). Distributions of $\alpha_{355}$ and $\alpha_{532}$ exhibit the largest values at the center of the flame base (0.00228 and 0.00221 $m^{-1}$, respectively), whereas $\alpha_{1064}$ is maximum (0.00064 $m^{-1}$) in a ring around the center of the flame base. In a sensitivity test performed on particle extinction coefficient, the uncertainties in the results varied between 18 and 20%, being larger at the bottom of the flame and smaller at the top. According to the literature, larger concentrations of soot particles are expected in this region in stable flames [20].

The relative differences among α at different wavelengths suggest the presence of different particle sizes along the monitored virtual matrix. Figure 8 (bottom row) shows AE in the spectral range 355-532 and 532-1064 nm, with larger values in the bottom of the flame than the top. $AE_{355\text{-}532}$ ranges between 0.64 and −0.36 and $AE_{532\text{-}1064}$ ranges between 3.86 (closest pixel to the emitter point) and −0.30, in the bottom and top of the flame, respectively. If a homogeneous size distribution function is assumed throughout the flame, AE indicates that the particles in the bottom (hot region) are smaller than those in the top (cold region), therefore suggesting that the nucleation and subsequent coagulation increases as distance from the emission point [21]. Nevertheless, Jung and Kim [22] show that AE is sensitive not only to particle size but also refractive index and therefore, variations in complex refractive index make more difficult to draw conclusions about the particle sizes from exclusively AE values. For mono-modal particle size distribution approximated by a lognormal function with small standard deviation (such as observed in industrial flares), they also reported negative AE values irrespective of the refractive index. However, these results can be used to define the homogeneous regions of the complex refractive index, which will be necessary to know for later retrieving the particle size distribution. According to the literature, it is possible to set the refractive index of the particles along the flame [23, 24]. These authors show that the refractive index distribution (especially its imaginary part) is dominantly influenced by the temperature in the flame. They also report that on the lean or rich side of a stoichiometric mixture ratio the refractive index is directly related to the progress of turbulent mixing and of the reaction process.

Several studies point out the relevance of the spectral variation of the Angström exponent (i.e. its curvature) to obtain information of the corresponding particle size distribution. Thus, using aerosol optical depth from sun-photometer as input data [25], reported that negative values of the AE spectral curvature (ΔAE) computed as $\Delta AE = AE_{440\text{-}613} - AE_{440\text{-}1003}$ indicate the predominance of fine mode aerosol, while positive differences indicate the effect of two separate modes with a significant coarse mode contribution. Schuster et al. [26] found that $AE_{670\text{-}870}$ is sensitive to the fine mode fraction (η, defined as the ratio between the fine-mode aerosol optical depth and the total aerosol optical depth), but not to the fine mode radius ($R_{fine}$). Conversely $AE_{340\text{-}440}$ is more sensitive to $R_{fine}$ but not to η. Gobbi et al. [27] proposed a simple graphical method to visually convert AE and ΔAE derived from sun-photometer to both $R_{fine}$ and η, and quality assured direct-sun data in the spectral range 400-870 nm retrieved from AERONET were used to demonstrate its feasibility. Recently [28], adapted

#221198 - $15.00 USD Received 18 Aug 2014; revised 25 Sep 2014; accepted 25 Sep 2014; published 8 Dec 2014

this method to the lidar community by using the wavelengths 355, 532 and 1064 nm and computing space (AE, ΔAE) based on particle extinction coefficients.

Our study takes advantage of the graphical network published by [28] computed for continental pollution with a refractive index of 1.445-0.0070i at 532 nm. Figure 9 shows the pairs $AE_{355\text{-}1064}$ and $\Delta AE = AE_{355\text{-}532}\text{-}AE_{532\text{-}1064}$ derived at each pixel of the virtual matrix where $\alpha_{1064} \geq 2.5 \cdot 10^{-4}$ $m^{-1}$. Particles in the hot region (defined as up to three pixels surrounding the emitter point) are mostly characterized by $R_{fine}$ between 0.15 and 0.25 μm and 50% < η < 100%. In contrast, particles in the cold region (defined as pixel located four or more pixels respect to the emitter point) showed smaller η with values shifting to mostly between 30% and 70%, revealing lower concentrations of fine particles as a consequence of the coarse mode particles generation by coagulation. Moreover, $R_{fine}$ seems to slightly decrease in the cold region, revealing a higher efficiency of the fine particles with larger sizes to coagulate.

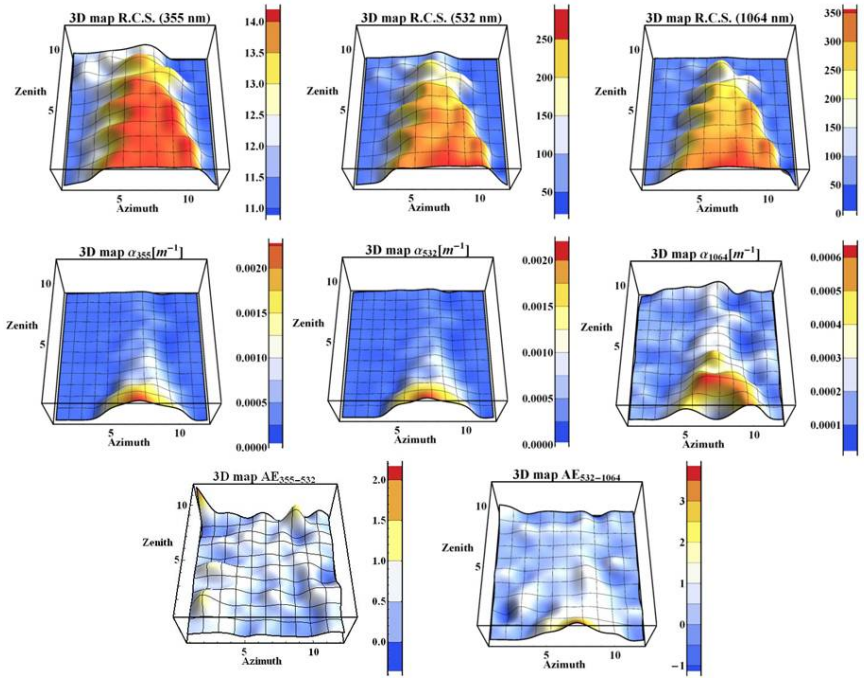


Fig. 8. Flame optical properties on the monitoring virtual matrix for different wavelengths and spectral ranges: (upper row) lidar R.C.S. in arbitrary units at 355, 532 and 1064 nm; (middle row) flame optical depth at 355, 532 and 1064 nm; and (bottom row) flame Angström Exponent at 355-532 nm and 532-1064 nm.

#221198 - $15.00 USD Received 18 Aug 2014; revised 25 Sep 2014; accepted 25 Sep 2014; published 8 Dec 2014

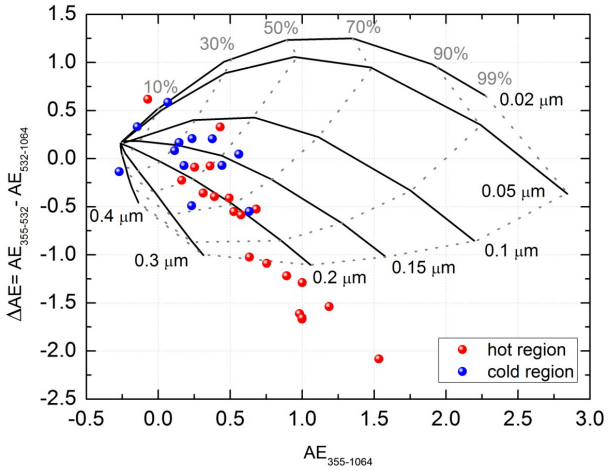


Fig. 9. Graphical network for aerosol characterization calculated by [28] for continental pollution.

## 5. Conclusions

In this work the electronic subsystem of a multiwavelength elastic scanning lidar placed at the industrial area of Cubatão in the State of São Paulo (Brazil) has been analyzed with the aim of improving the knowledge of its performance itself and designing protocols for correcting lidar signals for undesirable instrumental effects. The exhaustive characterization of the electronic subsystem (using several tests such as zero-bin, bin-shift and dark current at a set of different spatial resolutions) of the Cubatão scanning lidar revealed the need of implementing corrections before appropriately deriving trustable physical information of industrial flames. It was found a certain delay (asynchrony) between the laser pulse emission and start of data acquisition in analog (AN) mode for all wavelengths. To properly detect and range targets, some bins of the AN lidar signals must be removed, whose number is wavelength- and spatial resolution- dependent. The experimentally observed spatial resolution dependency agreed with the theoretically expected one. After investigating the bin-shift between AN and photoncounting (PC) signals, it was found synchronism in PC mode between the laser pulse emission and start of data acquisition for most of the selected spatial resolutions. However for 3.75-m spatial resolution, PC lidar signals must be corrected for uncorrected zero-bin position. Dark current measurements further revealed range-dependency very close to the instrument in the first 0.3 km, indicating a correction must be applied to get trustable lidar signals in this range. Therefore, due to the near field applications of this system, the dark current measurement in AN mode (measured before or after a real atmospheric measurement) must be subtracted to the lidar measurement.

A case study discussed in this manuscript illustrates the procedure to retrieve optical and microphysical properties of particles in flames. Besides the procedures applied to retrieve extinction and extinction-related Angström exponents, Gobbi's graphical method modified by [28] is applied for the first time to industrial flare research. This method, based on the space defined by the extinction-related Angström exponent versus its spectral curvature, proves a promising tool to obtain fine mode radius and fine mode fraction from lidar technique in industrial flames. This work demonstrates the capabilities of the multiwavelength elastic scanning lidar for industrial flare research (such as revealing features of the processes occurring inside the flame), being key for policy, impacts and decision-making, and also helping companies to improve the efficiency and compliance of their processes.

#221198 - $15.00 USD Received 18 Aug 2014; revised 25 Sep 2014; accepted 25 Sep 2014; published 8 Dec 2014

**Acknowledgments**

This work was supported by FAPESP (Fundação da Amparo à Pesquisa do Estado de São Paulo) through the visiting professor grant ref. 2013/21087-7 and projects 2011/14365-5 and 2008/58104-8; by the University of Granada through the contract "Plan Propio. Programa 9. Convocatoria 2013"; by the Spanish Ministry of Economy and Competitiveness through projects CGL2010-18782 and CGL2013-45410-R; and by the Andalusian Regional Government through projects P10-RNM-6299 and P12-RNM-2409. The authors want to thank to EARLINET and especially Prof. Freudenthaler for the huge effort to improve the instrumental knowledge in the lidar community.

#221198 - $15.00 USD Received 18 Aug 2014; revised 25 Sep 2014; accepted 25 Sep 2014; published 8 Dec 2014